ACS Energy LETTERS

http://pubs.acs.org/journal/aelccp

LETTER

Seed Layers for Wide-Band Gap Coevaporated Perovskite Solar Cells: CsCl Regulates Band Gap and Reduces Process Variability

Viktor Škorjanc,* Aleksandra Miaskiewicz, Marcel Roß,* Suresh Maniyarasu, Stefanie Severin, Matthew R. Leyden, Philippe Holzhey, Florian Ruske, Lars Korte, and Steve Albrecht*

Cite This: ACS Energy Lett. 2024, 9, 5639−5646

Read Online

ACCESS | Metrics & More | Article Recommendations | Supporting Information

ABSTRACT: Coevaporation, an up-scalable deposition technique that allows for conformal coverage of textured industrial silicon bottom cells, is particularly suited for application in perovskite-silicon tandem solar cells (PSTs). However, research on coevaporated perovskites with an appropriate band gap for PSTs remains limited, with lower efficiency and reproducibility than solution-processed films. Here, we present a simple approach using a thin layer of a precursor material, namely, PbI_2, $PbCl_2$, CsI, or CsCl, as a seed layer on the hole-transporting layer/perovskite interface. We find CsCl to be the optimal seed layer for our system. Perovskite single junction cells prepared with CsCl seed layer exhibit 19.6% power conversion efficiency with a band gap of 1.69 eV and improved long-term stability. We attribute the observed enhancements to the more precise and consistent incorporation of the organic precursor into the perovskite lattice during the film growth. This work demonstrates that engineering the substrate surface is crucial for achieving well-controlled growth of efficient and stable coevaporated wide-band gap perovskite solar cells.

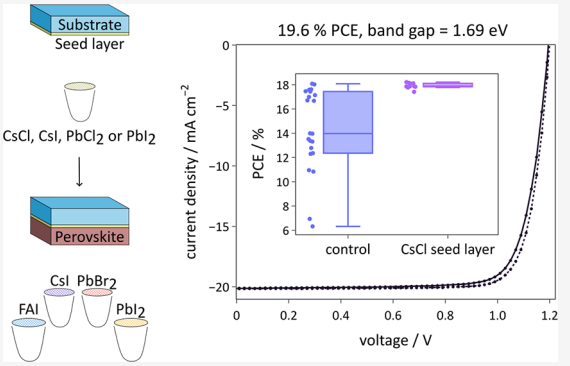

Metal halide perovskites have attracted considerable research interest over the past decade. Their high absorption coefficient,[1] charge-carrier diffusion lengths well above the typical film thickness of about 500 nm,[2,3] and high defect tolerance[4] make them particularly suitable for solar cells. Additionally, their band gap can be tuned by compositional engineering,[5,6] making them especially suitable for multijunction photovoltaics.

Perovskite-silicon tandem solar cells (PSTs) combine metal halide perovskites and silicon solar cells. Power conversion efficiencies (PCEs) of PSTs grew at an unprecedented rate since the early research efforts, now reaching 34.2%.[7] With a relative PCE gain of 25% compared to state-of-the art single-junction silicon counterparts, the transfer of this technology to industry becomes ever more relevant. However, scalable deposition techniques that yield homogeneous perovskite films and efficient PSTs are still lacking. Standard industrial silicon bottom cells have a textured surface with features up to 10 μm in size, exceeding the typical perovskite film thickness of about 500 nm. Achieving conformal coverage of such large features is challenging with solution-based deposition methods. Partial coverage of the surface can lead to the formation of shunts, negatively impacting solar cell device performance.[8,9] Vacuum deposition methods ensure conformal coverage of the textured surfaces of industrial silicon bottom cells, making them particularly appealing for PSTs.[10] In addition, these methods are solvent-free and provide good thickness control as well as homogeneous coverage of large substrates.

Most of the research in the field of perovskite photovoltaics focuses on solution-processed perovskites.[11] Nevertheless, a recent breakthrough pushed the efficiency of PSCs with sequentially evaporated perovskite film to 26.2% PCE,[12] which is equivalent to state-of-the-art solution-processed PSCs.[13] Despite the comparable record efficiency, research on evaporated perovskites remains limited, focusing on iodide-rich perovskites[11] with a band gap lower than the optimal value of ∼1.68 eV for PSTs.[14] The highest reported efficiency for a vacuum-processed single-junction solar cell with 1.68 eV band gap is 17.6%,[15] while the most efficient PSTs with fully evaporated perovskite film reached 27.4%.[16] Both values are far

Received: August 8, 2024
Revised: October 1, 2024
Accepted: October 22, 2024
Published: October 31, 2024

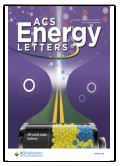

https://doi.org/10.1021/acsenergylett.4c02173
ACS Energy Lett. 2024, 9, 5639−5646

below those for state-of-the-art solution-processed PSTs. Thus, additional research is needed to close the gap between solution- and vacuum-processed perovskites in PSTs. Another major challenge is the limited process reproducibility—two deposition runs can yield significantly different films even though the process parameters were the same.[17] In case of quartz-crystal-microbalance (QCM)-controlled processes, poor reproducibility can originate from discrepancy between the precursor sticking coefficient on the substrate and the QCM,[18] as well as a low sticking coefficient on the QCM.[19] In addition, precursor degradation[20,21] and impurities[18,22] can limit process reproducibility.

Controlling the film growth is a key step in achieving highly efficient and stable PSCs with evaporated perovskite films. The early stage of film growth is particularly important, as it defines an initial structure atop of which further layers are deposited. Surface properties of the substrate on which the film is grown thereby have a strong impact on the film morphology, composition, and optoelectronic properties.[20,23−28] This limits which charge-selective layers can be used at the buried interface, making the development of perovskites more challenging. Abzieher et al.[23] found that coevaporated perovskite films initially grow in island mode, with further lateral film growth influenced by the substrate's polarity. Substrates covered with nonpolar organic compounds favor columnar growth, in contrast to substrates covered with metal oxides or polar organic compounds. Columnar growth reduces the number of horizontal grain boundaries, which represent charge transfer bottlenecks.[29,30]

In addition to changes to the film morphology, the substrate material can also influence the incorporation of precursor into the perovskite film. Methylammonium iodide (MAI) and formamidinium iodide (FAI) are the most-used organic precursors in vacuum-processed perovskite films. Emission of their vapor from the evaporation source is not purely ballistic; it resembles chemical vapor deposition as the molecules can dissociate upon sublimation and reassociate at the substrate surface.[20−22] This makes the incorporation of the organic precursors particularly sensitive to processing parameters, such as pressure,[31] substrate temperature,[24] and substrate material used. Less polar substrates favor the incorporation of organic precursors.[23,24] Bækbo et al.[20] showed that the MAI sticking coefficient increases when the substrate is covered by a thin $PbCl_2$ layer, as the energetically favorable perovskite formation aids MAI deposition. Similarly, in the case of $MAPbI_3$ coevaporation, PbI_2 initially forms at the interface.[26,27,31] The thin PbI_2 layer then supports the incorporation of MAI. Heinze et al.[31] deposited up to 20 nm thick PbI_2 layer on the substrate by delaying the start of MAI deposition, thus achieving higher perovskite film crystallinity and improved solar cell performance. Notably, Rothmann et al. indicated that PbI_2 can smoothly incorporate into the perovskite material without interrupting the perovskite structure, which explains why it can be beneficial as a seed layer.[32] Overall, the research so far suggests that PbI_2 can act as a seed for perovskite growth and still facilitate efficient charge transport. However, it was also found that unreacted PbI_2 can negatively influence the stability of solution-processed films.[33,34] It is not clear whether the negative impact of PbI_2 on the stability is true for evaporated films.

In an effort to mitigate the sensitivity to the substrate, Yan et al.[28] introduced a 15 nm thick sequentially deposited metal halide perovskite templating layer by three-source coevaporation of the inorganic components (PbI_2, CsI, and $PbCl_2$) followed by evaporation of FAI and annealing of the templating film, prior to coevaporating $FA_{0.9}Cs_{0.1}PbI_{3-x}Cl_x$ perovskite atop. While this method involves a more complex processing step, it shows how the sensitivity of the film growth to the substrate surface properties can be reduced by controlling the composition of the initial perovskite layer.

Recently, some of the high-efficiency reported perovskite solar cells used a hybrid fabrication route, highlighting that the challenge with evaporation processing is the incorporation of organic components. Li et al. found that for $FA_{0.9}Cs_{0.1}PbI_{2.87}Br_{0.13}$ hybrid-deposited perovskite with band gap of around 1.65 eV, a 5 nm thick CsBr[35] layer at the buried hole-transporting layer (HTL)-perovskite interface was beneficial for the performance of PSTs by mitigating the effect of residual PbI_2 at the interface.

In summary, one of the main challenges for evaporated perovskites is homogeneous incorporation of the organic component throughout the perovskite film, which can be influenced by modifying the substrate surface. Seed layers were already used to control film formation but rarely systematically investigated. In addition, few studies reported evaporated films relevant for PSTs with bandgaps between 1.64 to 1.70 eV.

Here, we investigate the effect of four perovskite precursors, namely, PbI_2, $PbCl_2$, CsI, and CsCl, as seed layers on growth of coevaporated perovskites for PST application. Applying the seed layer is straightforward, requiring a single deposition step without postdeposition annealing. The perovskite film is deposited onto the seed layers using four-source coevaporation in high vacuum, with PbI_2, $PbBr_2$, CsI, and FAI as precursors. More information about the development of the four-source perovskite deposition method is available in Supplementary Note 1. In this study, we link the morphological and compositional changes to changes in optoelectronic properties and PSC performance. We show how Cs-containing seed layers can improve the inclusion of FAI. The seed layers modify the film band gap, reduce the variability of film optoelectronic properties within a deposition run, and influence the performance of solar cell devices. PSCs with optimized CsCl seed layer thickness reach 19.6% PCE with 1.69 eV band gap. In addition, PSCs with a CsCl seed layer show excellent stability, with no loss in PCE after 1000 h of maximum power point tracking (MPPT) at 25 °C in N_2 under constant AM 1.5 G illumination.

We deposited 10 nm of seed layers on glass/indium−tin oxide (ITO)/MeO-2PACz substrates and coevaporated $(FA_{0.94}Cs_{0.20})Pb(I_{0.94}Br_{0.11})_3$ atop. The films were then annealed at 180 °C for 5 min. Figure 1A-E shows cross-sectional scanning electron microscope (SEM) images of perovskite films grown on top of substrates with 10 nm thick seed layers. The perovskite films originate from the same deposition run. Since we observed a large spread in the properties of the control films grown without a seed layer in this deposition run, we show the analysis of two control samples, one with a large band gap (light blue) and one with a narrow band gap (dark blue), to give a comprehensive representation of the complete data set. Data from this deposition run are also presented in Figure 2 and 3B, while in data presented in Figure S3 we did not observe such a variation due to a smaller sample size; therefore, one control sample is shown. We do not know the exact cause for the variation and believe that it arises from subtle differences between the substrates, potentially due to an uncontrolled factor, such as

https://doi.org/10.1021/acsenergylett.4c02173
ACS Energy Lett. 2024, 9, 5639−5646

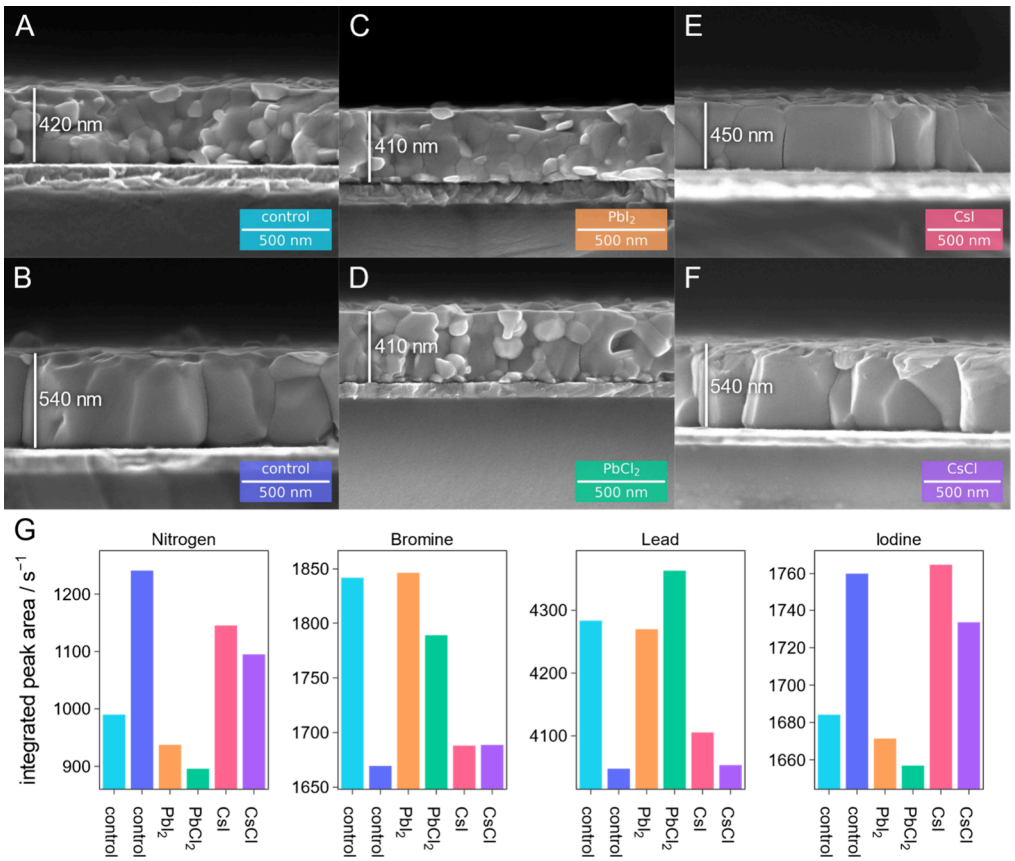

Figure 1. Impact of 10 nm seed layer on morphology and composition of coevaporated $(FA_{0.94}Cs_{0.20})Pb(I_{0.94}Br_{0.11})_3$ films deposited in the same perovskite coevaporation run. All films were deposited on glass/ITO/MeO-2PACz[/seed layer] and annealed postdeposition at 180 °C for 5 min in N_2. Cross-sectional SEM images of control films without a seed layer (A, B) and films grown atop of 10 nm PbI_2 (C), $PbCl_2$ (D), CsI (E), and CsCl (F) seed layers. Vertical bars indicate the approximate thickness of the perovskite layer. (G) Integrated EDX peak area of nitrogen, bromine, lead, and iodine peak for samples shown in A-F.

slight variations in glovebox conditions during the MeO-2PACz spin-coating, as one possible example. SEM images highlight a stark contrast in the morphologies of the two nominally identical control films (Figure 1A,B). Films without seed layer can feature large apparent grains (Figure 1B) but also much smaller grain sizes (Figure 1A). Films grown on PbI_2 and $PbCl_2$ (Figure 1C,D) show a morphology with small apparent grains. In addition, SEM images indicate that a distinct thin layer might be present at the HTL-perovskite interface, which could indicate that the seed layer is not fully intermixed with the film bulk. A separate phase at the interface can act as a charge extraction barrier or create trap states, with a negative impact on solar cell device properties.[36] Contrary to the films grown on PbI_2 and $PbCl_2$, films grown on CsI and CsCl (Figure 1E,F) exhibit large apparent grains, extending from the substrate to the surface. Since grain boundaries perpendicular to the growth direction are known to be charge extraction bottlenecks,[29,30] having no grain boundaries between the HTL and the ETL is expected to bolster charge extraction. No distinct layer is visible at the interface, indicating that the seed layer intermixes with the perovskite film. It is important to note that films with large apparent grains are also thicker than those with small apparent grains, which is unexpected, given that they were prepared in the same deposition run. This observation suggests that one or more precursors are incorporated to a greater extent into the thicker films with large apparent grains. However, the film with CsI seed layer is an exception, where due to a high nitrogen content, a higher thickness would be expected, but a thinner film is observed. We note that the cross-sectional SEM images capture only a small portion of the sample, and some degree of local variation in thickness is expected, which may explain the different result for CsI seed layer. Figure S1 shows images of not-annealed films from another deposition run. While there is a subtle difference in the morphology of the films prior to annealing, it is not as pronounced as for annealed films.

Figure S2 shows energy dispersive X-ray spectroscopy (EDX) spectra for the samples shown in Figure 1A-F. Figure 1G shows integrated peak areas for nitrogen (N Kα1,2, 0.33−0.43 keV), bromine (Br Lα1,2, 1.41−1.59 keV), lead (Pb Mα1, Mβ, 2.25−2.55 keV), and iodine (I Lα1, 3.82−4.04 keV) peaks. EDX analysis details are provided in Supplementary Note 2. It can be noted that compared to the Pb-based seed layers, films grown on Cs-based seed layers have more nitrogen and iodine, indicating better incorporation of FAI into the films. The increased nitrogen content and iodine content for samples with CsI and CsCl seed layers, as well as for one control sample without a seed layer, are correlated with large apparent grains visible in the SEM images. Higher incorporation of FAI could thus explain the higher thickness of the samples with large apparent grains.[37] The samples that are poor in nitrogen and iodine are rich in lead and bromine. The fraction of bromine correlates well with the changes in band gap of material shown in Figure 2. The two control samples

https://doi.org/10.1021/acsenergylett.4c02173
ACS Energy Lett. 2024, 9, 5639−5646

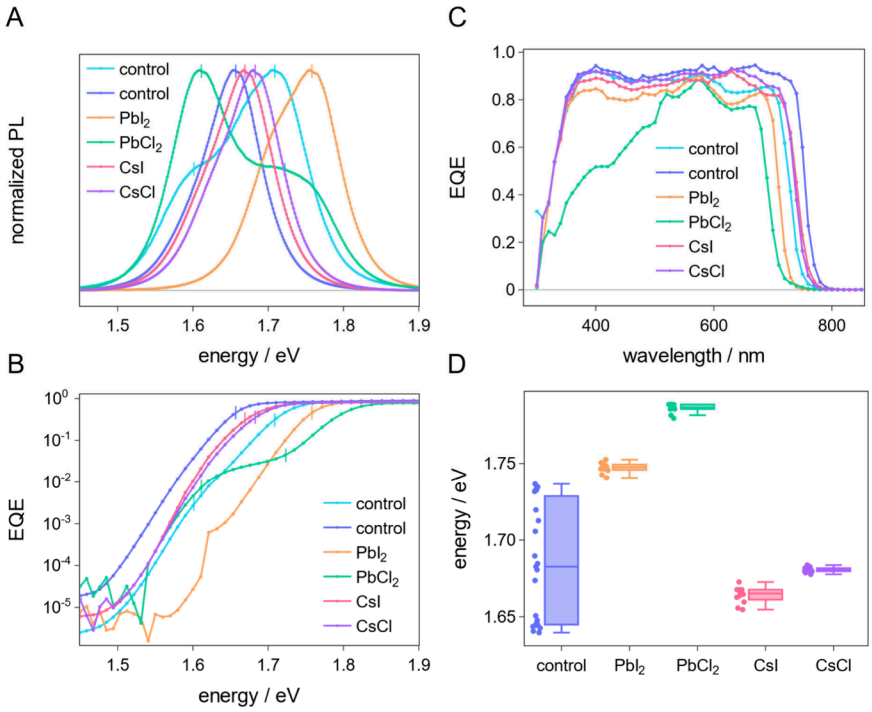

Figure 2. Optoelectronic properties of films with and without seed layer from the same perovskite coevaporation deposition run. The samples were annealed at 180 °C for 5 min in N_2. PL spectra were measured on glass/ITO/MeO-2PACz[/seed layer]/perovskite, while the complete solar cells used in the EQE measurements also have C_{60}/BCP/Ag on top of the perovskite. (A) PL spectra. (B) Sensitive EQE spectra. The artifact at ∼1.62 eV visible for the PbI_2 seeded film is caused by a filter change. Vertical lines in subfigures A and B indicate the position of the PL peak maxima. (C) EQE spectra. (D) Distribution of band gap values calculated from EQE spectra.

have pronounced compositional differences, indicating an increased probability of compositional variation in films grown without a seed layer. The morphological and compositional variations of control films reflect in the optoelectronic properties and PSC device performance, as discussed below (Figures 2 and 3B).

To better understand the observed compositional differences, we analyzed the composition of the film surface of not-annealed perovskite films of various thicknesses by X-ray photoemission spectroscopy (XPS) and compared it with X-ray diffraction (XRD) measurements. The results confirm that Cs-based seed layers foster the incorporation of the organic precursor FAI. XPS and XRD data are shown in Figure S3 and discussed in detail in Supplementary Note 3.

The observed differences in morphology and composition between films grown on a seed layer and control films reflect their optoelectronic properties. Figure 2A shows the normalized photoluminescence (PL) spectra for films grown on glass/ITO/MeO-2PACz, with and without a seed layer. Depending on the seed layer, the position of the PL maximum, labeled by a vertical line, is shifted, indicating a difference in the films' band gap. If the sample featured a shoulder in the spectrum, the position of the maxima was estimated by fitting a double-Gaussian curve (see Figure S7). The positions of the PL maxima are also indicated on the sensitive EQE spectra, shown in Figure 2B, measured on finished cells (cf. Figure 3A), demonstrating that the band gaps are in good agreement between the two measurements. The extent of band gap shift is surprising given that only 10 nm of seed layer was deposited underneath an ∼500 nm thick perovskite film. The photoluminescence quantum yield (PLQY) is also influenced by the seed layer used, with the samples with CsI and CsCl seed layers showing the highest PLQY and quasi-Fermi level splitting (QFLS) values (see non-normalized PL spectra in Figure S8 and PLQY and QFLS values in Table S2). Full EQE spectra (Figure 2C) show parasitic absorption at wavelengths below 500 nm for a film with a $PbCl_2$ seed layer, which we attribute to the excess PbI_2. PL and EQE spectra presented in Figure 2A-C are discussed in greater detail in Supplementary Note 4.

To determine the distribution of band gap values for different films, we measured EQE spectra of ten or more PSCs per variation in the narrow region of 850−650 nm around the inflection point. EQE measurements used to calculate data shown in Figure 2D are shown in Figure S9, together with PL measurements for all measured samples. The distribution of band gap values of films grown on different seed layers and without a seed layer, all deposited within the same deposition run, is shown in Figure 2D. Films grown without a seed layer exhibit a large variation in the band gap values, whereas films grown with a seed layer show narrow distributions. This indicates that the seed layers can be used not only to regulate the band gaps of the films but also to substantially reduce the variability of their optoelectronic properties. It is important to note that films grown atop of CsCl have a band gap of 1.68 eV, the optimal value for perovskite-silicon tandem cell application.

Figure 3A shows the solar cell stack used in this work, and Figure 3B shows the distribution of parameters extracted from current voltage (J−V) measurements of PSCs on different seed layers. We prepared the devices within the same deposition run as for the samples shown in Figures 1 and 2. Although the maximum efficiency of samples without and with CsCl seed layer are comparable, there is much higher variation in the values measured for the control samples. This is consistent

https://doi.org/10.1021/acsenergylett.4c02173
ACS Energy Lett. 2024, 9, 5639−5646

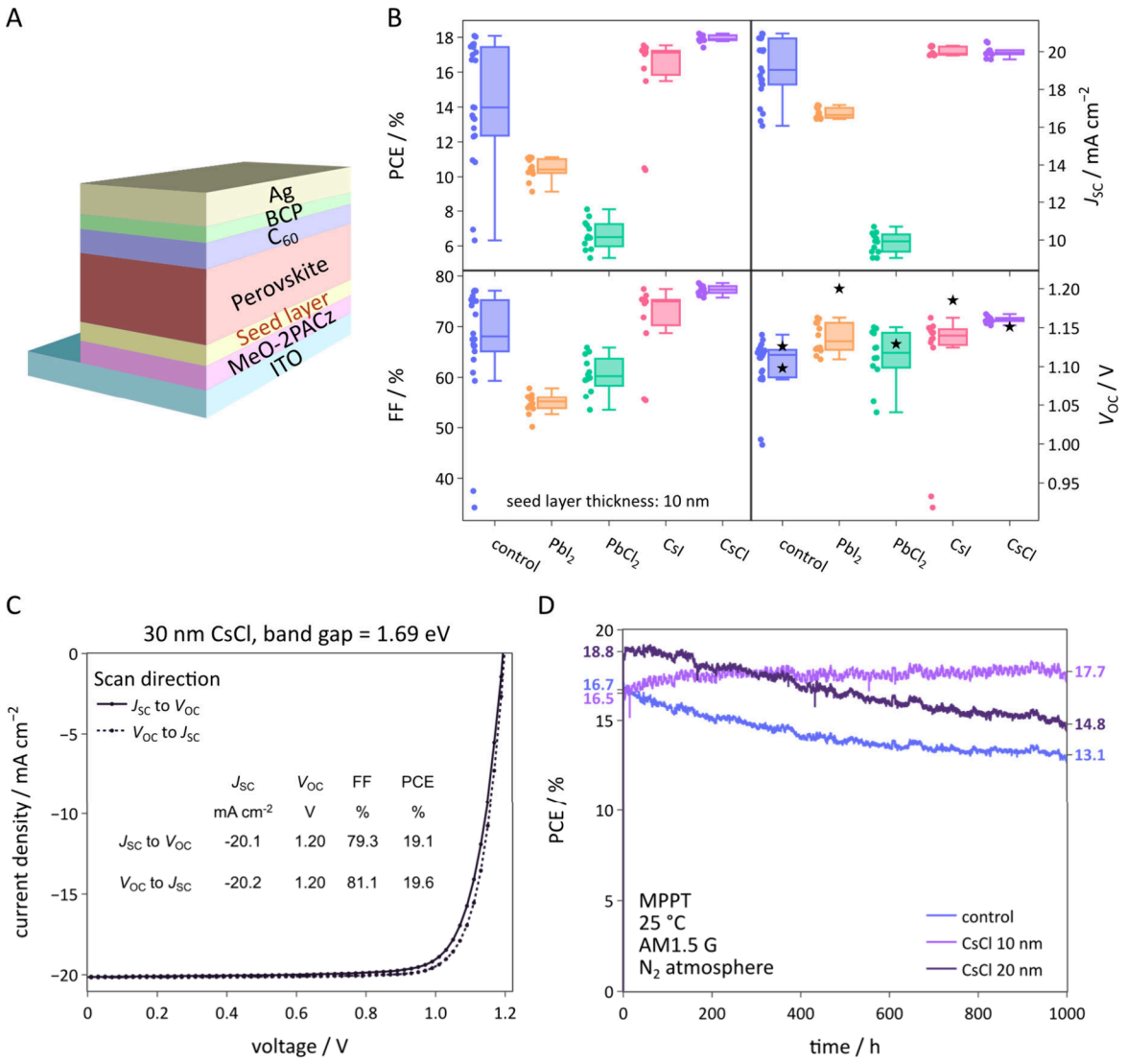

Figure 3. Solar cell performance and stability measurements under simulated AM 1.5G illumination. (A) Schematic of the device stack. (B) Statistical distribution of PCE, short-circuit current (J_{SC}), fill factor (FF), and open-circuit voltage (V_{OC}) values. The presented data are average values of the forward and reverse scans. QFLS values calculated from the high-energy tail fits of corresponding PL spectra are represented in the V_{OC} panel as black stars. (C) J–V curve of a selected best-efficiency device with 30 nm CsCl seed layer, with a LiF antireflection layer on the glass side. (D) PCE measured by constant MPPT during 1000 h of AM1.5-G-equivalent illumination at 25 °C in a N_2 atmosphere. The rear (nonilluminated) surface of the devices was coated with a 30 nm thick Al_2O_3 film prior to the stability measurements. The initial and final PCE are labeled on the left and right sides of the Y axis, respectively.

with the variation in the band gap shown in Figure 2D, as well as the differences in the morphology and composition indicated in Figure 1. Devices without a seed layer that exhibit high PCE also have high J_{SC}, consistent with the lower band gap measured for some of these samples. However, the samples without a seed layer have a lower V_{OC} value compared to samples grown on CsCl, resulting in similar PCE values. Further, devices with CsCl have a higher band gap, which is better suited for tandem application than for the single-junction cells shown here. Devices with lead-based seed layers have a lower J_{SC} and fill factor (FF), as well as a high spread in V_{OC}, which is consistent with the smaller size of apparent grains, shown in Figure 1C,D, as well as the phase heterogeneity visible in the PL and EQE spectra shown in Figure 2A,C. It is important to note that we observed an improvement in efficiencies for devices stored in N_2 with time. The data in Figure 3B was measured 2 months after device fabrication on a subset of initially fabricated solar cells. Figure S10 shows the efficiency of all the fabricated PSCs 1 day after deposition.

With these findings, we selected CsCl as the optimal seed layer for further optimization and then varied the CsCl thickness. Figure S11 shows top-view SEM images of 10, 20, and 30 nm thick CsCl seed layers, as well as an estimate of the fraction of the substrate covered by the seed layer. As the thickness of the CsCl seed layer increases from 10 to 20 nm, the fraction of the substrate covered by seed layer increases from around 40 to 70%, with a change in the seed layer morphology from islands to an interconnected perforated film. 30 nm thick film covers a similar fraction of the substrate as the 20 nm thick film; however, the CsCl domains are larger and more well-defined. In addition to morphological differences, increasing the thickness of CsCl introduces additional Cs^+ and Cl^- ions, which are known to increase the band gap of the

https://doi.org/10.1021/acsenergylett.4c02173
ACS Energy Lett. 2024, 9, 5639−5646

perovskite film.[38,39] We noticed that seed layers thicker than 10 nm can be beneficial for reproducible band gap control while not hindering the device efficiency. Figure S12 shows the results of a deposition run where the thickness of the CsCl layer was optimized. The devices with 30 nm thick CsCl layer have on average the highest V_{OC} and FF but also a lower J_{SC} than devices with 20 nm CsCl. While the PSCs with 20 nm thick CsCl layer yielded on average the highest PCE, the champion cell (Figure 3C) features a 30 nm CsCl layer and a band gap of 1.69 eV. This device reaches an outstanding V_{OC} for coevaporated perovskites of 1.20 V, with a high FF of ∼80% and low hysteresis, resulting in 19.6% and 19.1% efficiency for the forward and reverse scan, respectively. EQE spectrum of the champion cell is shown in Figure S13. Figure S14 shows *JV* data from 3 different deposition runs for control samples and samples with 20 nm CsCl. While there remains some variation between deposition runs, CsCl regularly reduces the variability of the control devices and increases efficiency.

We measured the stability of PSCs without a seed layer, with 10 nm and 20 nm thick CsCl seed layer under maximum power point tracking (MPPT) with continuous AM1.5-G-equivalent illumination without a UV filter in a N_2 atmosphere. Figure 3D shows the best-performing PSCs, while Figure S15 shows the statistical distribution. The cells' rear side was coated with 30 nm thick Al_2O_3 layer as an encapsulant prior to the stability measurements to prevent outgassing of the volatile components.[40,41] While the solar cell devices without seed layer (T_{80} = 790 h) and with 20 nm CsCl (T_{80} = 1000 h) show similar degradation behavior, devices with 10 nm CsCl show no degradation during the MPP-tracking (PCE 1.2% higher at the end compared with the beginning of the measurement). It is important to note that in this deposition run the solar cell devices without a seed layer featured a band gap of 1.63 eV, increasing to 1.64 eV with 10 nm CsCl and 1.68 eV for 20 nm thick CsCl layer. Possible causes for band gap variation are discussed in Supplementary Note 5. Overall, the thicker templates, while beneficial for the device efficiency, might not benefit device stability. It is also possible that this variation is a result of statistical variation. The stability aspect needs further investigation.

We measured MPPT on the same devices with a 10 nm CsCl layer at an elevated temperature, 65 °C. Figure S16A shows the best-performing PSC, while Figure S16B shows the statistical distribution. The best-performing device had a T_{80} of 1030 h. This exceptional stability is even more impressive given that the PSCs had already undergone MPPT at 25 °C for 1000 h. The remarkable durability of our devices underscores the potential of this technology for real-world application.

It becomes clear that one of the main challenges of coevaporated perovskites is the bottom substrate. The layer evaporated on top is crucial for the properties of the consecutive layer. Herein, we establish a seed layer approach with simple and commonly available salts: PbI_2, $PbCl_2$, CsI, and CsCl. Especially, CsI and CsCl (both cubic structures) as seed layers yield perovskite films with large apparent grain size and favor incorporation of the organic precursor FAI. In contrast, films with PbI_2 and $PbCl_2$ feature small apparent grains and a low fraction of the organic precursor. Furthermore, films without seed layer showed a strong variation in the optoelectronic properties, likely caused by an increased compositional variation during the initial phase of film growth at the surface without a seed layer. The seed layers reduce these variations considerably and modify the film growth and cation incorporation, which changes the band gap of the material. Films with CsCl seed layer show a band gap of 1.68 eV, a value well-suited for PST application. In addition, the samples with CsCl yield PSCs with a higher FF and V_{OC} compared to samples without a seed layer, with a comparable J_{SC} despite a higher band gap. Upon increasing the CsCl thickness to 30 nm, the PSC reached 19.6% PCE in p-i-n architecture, with a band gap of 1.69 eV. PSCs with CsCl also show superior stability compared to samples without a seed layer, with no decrease in efficiency after 1000 h of MPP tracking under constant AM1.5 G illumination at 25 °C in N_2 atmosphere. Thus, we have demonstrated that a simple and straightforward step decreases process variability and enhances device efficiency and stability of coevaporated wide-band gap perovskites for tandem application.

■ ASSOCIATED CONTENT

Supporting Information

The Supporting Information is available free of charge at https://pubs.acs.org/doi/10.1021/acsenergylett.4c02173.

Additional details about experimental methods, SEM, EDX, XPS, XRD, PL, EQE, solar cell efficiency and stability data (PDF)

■ AUTHOR INFORMATION

Corresponding Authors

Viktor Škorjanc − *Helmholtz-Zentrum Berlin für Materialien und Energie, Division Solar Energy, 14109 Berlin, Germany;* orcid.org/0000-0002-2438-0090; Email: viktor.skorjanc@helmholtz-berlin.de

Marcel Roß − *Helmholtz-Zentrum Berlin für Materialien und Energie, Division Solar Energy, 14109 Berlin, Germany;* orcid.org/0000-0002-5916-8540; Email: marcel.ross@helmholtz-berlin.de

Steve Albrecht − *Helmholtz-Zentrum Berlin für Materialien und Energie, Division Solar Energy, 14109 Berlin, Germany; Faculty of Electrical Engineering and Computer Science, Technical University Berlin, 10587 Berlin, Germany;* orcid.org/0000-0001-9962-9535; Email: steve.albrecht@helmholtz-berlin.de

Authors

Aleksandra Miaskiewicz − *Helmholtz-Zentrum Berlin für Materialien und Energie, Division Solar Energy, 14109 Berlin, Germany*

Suresh Maniyarasu − *Helmholtz-Zentrum Berlin für Materialien und Energie, Division Solar Energy, 14109 Berlin, Germany*

Stefanie Severin − *Helmholtz-Zentrum Berlin für Materialien und Energie, Division Solar Energy, 14109 Berlin, Germany*

Matthew R. Leyden − *Helmholtz-Zentrum Berlin für Materialien und Energie, Division Solar Energy, 14109 Berlin, Germany*

Philippe Holzhey − *Helmholtz-Zentrum Berlin für Materialien und Energie, Division Solar Energy, 14109 Berlin, Germany*

Florian Ruske − *Helmholtz-Zentrum Berlin für Materialien und Energie, Division Solar Energy, 14109 Berlin, Germany*

Lars Korte − *Helmholtz-Zentrum Berlin für Materialien und Energie, Division Solar Energy, 14109 Berlin, Germany;* orcid.org/0000-0002-9207-9048

Complete contact information is available at:
https://pubs.acs.org/10.1021/acsenergylett.4c02173

Author Contributions

V.Š., M.R., and A.M. planned the experiments and coordinated the work. A.M., V.Š., M.R., S.S., and M.R.L. prepared the films for the analysis and processed the single-junction cells. A.M. conducted the JV, EQE, SEM, and EDX measurements. V.Š. conducted the XRD, PL, and sensitive EQE measurements. V.Š. and P.H. analyzed the XRD measurements. V.Š., A.M., and F.R. analyzed the EDX measurements. S.M. conducted and analyzed the XPS experiments. S.A., L.K., and M.R. supervised the project. V.Š. prepared the figures. All authors contributed to data interpretation and manuscript writing.

Notes

The authors declare no competing financial interest.

■ ACKNOWLEDGMENTS

The authors acknowledge funding from the Helmholtz Association within the HySPRINT Innovation lab project, the *Zeitenwende* project, and the HyPerCells joint Research School between HZB and University of Potsdam, SHAPE (grant no. 03EE1123C), and PrESTO (grant no. 03EE1086C) funded by the Federal Ministry of Economy and Climate Action (BMWK). The Energy Materials In-situ Laboratory Berlin (EMIL) operated by the Helmholtz-Zentrum für Materialien und Energie GmbH (HZB) is acknowledged for granting access to its sample characterization laboratory. Authors thank the department Active Materials and Interfaces for Stable Perovskite Solar Cells, T. W. Gries, J. M. Beckedahl, and A. Abate for High-throughput Ageing Setup measurements and the Photovoltaics Competence Center Berlin, Hajar Mourine for the assistance with Al_2O_3 deposition.

■ REFERENCES

(1) De Wolf, S.; Holovsky, J.; Moon, S.-J.; Löper, P.; Niesen, B.; Ledinsky, M.; Haug, F.-J.; Yum, J.-H.; Ballif, C. Organometallic Halide Perovskites: Sharp Optical Absorption Edge and Its Relation to Photovoltaic Performance. *J. Phys. Chem. Lett.* **2014**, *5* (6), 1035−1039.

(2) Xing, G.; Mathews, N.; Sun, S.; Lim, S. S.; Lam, Y. M.; Grätzel, M.; Mhaisalkar, S.; Sum, T. C. Long-Range Balanced Electron- and Hole-Transport Lengths in Organic-Inorganic $CH_3NH_3PbI_3$. *Science* **2013**, *342* (6156), 344−347.

(3) Herz, L. M. Charge-Carrier Mobilities in Metal Halide Perovskites: Fundamental Mechanisms and Limits. *ACS Energy Lett.* **2017**, *2* (7), 1539−1548.

(4) Ball, J. M.; Petrozza, A. Defects in Perovskite-Halides and Their Effects in Solar Cells. *Nat. Energy* **2016**, *1* (11), 1−13.

(5) Tanaka, K.; Takahashi, T.; Ban, T.; Kondo, T.; Uchida, K.; Miura, N. Comparative Study on the Excitons in Lead-Halide-Based Perovskite-Type Crystals $CH_3NH_3PbBr_3$ $CH_3NH_3PbI_3$. *Solid State Commun.* **2003**, *127* (9), 619−623.

(6) Noh, J. H.; Im, S. H.; Heo, J. H.; Mandal, T. N.; Seok, S. I. Chemical Management for Colorful, Efficient, and Stable Inorganic-Organic Hybrid Nanostructured Solar Cells. *Nano Lett.* **2013**, *13* (4), 1764−1769.

(7) Green, M. A.; Dunlop, E. D.; Yoshita, M.; Kopidakis, N.; Bothe, K.; Siefer, G.; Hinken, D.; Rauer, M.; Hohl-Ebinger, J.; Hao, X. Solar Cell Efficiency Tables (Version 64). *Prog. Photovolt. Res. Appl.* **2024**, *32* (7), 425−441.

(8) Chen, B.; Yu, Z. J.; Manzoor, S.; Wang, S.; Weigand, W.; Yu, Z.; Yang, G.; Ni, Z.; Dai, X.; Holman, Z. C.; Huang, J. Blade-Coated Perovskites on Textured Silicon for 26%-Efficient Monolithic Perovskite/Silicon Tandem Solar Cells. *Joule* **2020**, *4* (4), 850−864.

(9) Hou, Y.; Aydin, E.; De Bastiani, M.; Xiao, C.; Isikgor, F. H.; Xue, D.-J.; Chen, B.; Chen, H.; Bahrami, B.; Chowdhury, A. H.; Johnston, A.; Baek, S.-W.; Huang, Z.; Wei, M.; Dong, Y.; Troughton, J.; Jalmood, R.; Mirabelli, A. J.; Allen, T. G.; Van Kerschaver, E.; Saidaminov, M. I.; Baran, D.; Qiao, Q.; Zhu, K.; De Wolf, S.; Sargent, E. H. Efficient Tandem Solar Cells with Solution-Processed Perovskite on Textured Crystalline Silicon. *Science* **2020**, *367* (6482), 1135−1140.

(10) Gil-Escrig, L.; Roß, M.; Sutter, J.; Al-Ashouri, A.; Becker, C.; Albrecht, S. Fully Vacuum-Processed Perovskite Solar Cells on Pyramidal Microtextures. *Sol. RRL* **2021**, *5* (1), 2000553.

(11) Kosasih, F. U.; Erdenebileg, E.; Mathews, N.; Mhaisalkar, S. G.; Bruno, A. Thermal Evaporation and Hybrid Deposition of Perovskite Solar Cells and Mini-Modules. *Joule* **2022**, *6* (12), 2692−2734.

(12) Zhou, J.; Tan, L.; Liu, Y.; Li, H.; Liu, X.; Li, M.; Wang, S.; Zhang, Y.; Jiang, C.; Hua, R.; Tress, W.; Meloni, S.; Yi, C. Highly Efficient and Stable Perovskite Solar Cells via a Multifunctional Hole Transporting Material. *Joule* **2024**, *8* (6), 1691−1706.

(13) Chen, H.; Liu, C.; Xu, J.; Maxwell, A.; Zhou, W.; Yang, Y.; Zhou, Q.; Bati, A. S. R.; Wan, H.; Wang, Z.; Zeng, L.; Wang, J.; Serles, P.; Liu, Y.; Teale, S.; Liu, Y.; Saidaminov, M. I.; Li, M.; Rolston, N.; Hoogland, S.; Filleter, T.; Kanatzidis, M. G.; Chen, B.; Ning, Z.; Sargent, E. H. Improved Charge Extraction in Inverted Perovskite Solar Cells with Dual-Site-Binding Ligands. *Science* **2024**, *384* (6692), 189−193.

(14) Jošt, M.; Köhnen, E.; Morales-Vilches, A. B.; Lipovšek, B.; Jäger, K.; Macco, B.; Al-Ashouri, A.; Krč, J.; Korte, L.; Rech, B.; Schlatmann, R.; Topič, M.; Stannowski, B.; Albrecht, S. Textured Interfaces in Monolithic Perovskite/Silicon Tandem Solar Cells: Advanced Light Management for Improved Efficiency and Energy Yield. *Energy Environ. Sci.* **2018**, *11* (12), 3511−3523.

(15) Chiang, Y.-H.; Frohna, K.; Salway, H.; Abfalterer, A.; Pan, L.; Roose, B.; Anaya, M.; Stranks, S. D. Vacuum-Deposited Wide-Bandgap Perovskite for All-Perovskite Tandem Solar Cells. *ACS Energy Lett.* **2023**, *8* (6), 2728−2737.

(16) Xu, Y.-Y.; Jiang, Y.; Du, H.-Q.; Gao, X.; Qiang, Z.-Y.; Wang, C.-X.; Tao, Z.-W.; Yang, L.-H.; Zhi, R.; Liang, G.-J.; Cai, H.-Y.; Rothmann, M. U.; Cheng, Y.-B.; Li, W. Octahedral Tilt Enables Efficient and Stable Fully Vapor-Deposited Perovskite/Silicon Tandem Cells. *Adv. Funct. Mater.* **2024**, *34* (11), 2312037.

(17) Abzieher, T.; Moore, D. T.; Roß, M.; Albrecht, S.; Silvia, J.; Tan, H.; Jeangros, Q.; Ballif, C.; Hoerantner, M. T.; Kim, B.-S.; Bolink, H. J.; Pistor, P.; Goldschmidt, J. C.; Chiang, Y.-H.; Stranks, S. D.; Borchert, J.; McGehee, M. D.; Morales-Masis, M.; Patel, J. B.; Bruno, A.; Paetzold, U. W. Vapor Phase Deposition of Perovskite Photovoltaics: Short Track to Commercialization? *Energy Environ. Sci.* **2024**, *17* (5), 1645−1663.

(18) Borchert, J.; Levchuk, I.; Snoek, L. C.; Rothmann, M. U.; Haver, R.; Snaith, H. J.; Brabec, C. J.; Herz, L. M.; Johnston, M. B. Impurity Tracking Enables Enhanced Control and Reproducibility of Hybrid Perovskite Vapor Deposition. *ACS Appl. Mater. Interfaces* **2019**, *11* (32), 28851−28857.

(19) Pistor, P.; Borchert, J.; Fränzel, W.; Csuk, R.; Scheer, R. Monitoring the Phase Formation of Coevaporated Lead Halide Perovskite Thin Films by in Situ X-Ray Diffraction. *J. Phys. Chem. Lett.* **2014**, *5* (19), 3308−3312.

(20) Bækbo, M. J.; Hansen, O.; Chorkendorff, I.; Vesborg, P. C. K. Deposition of Methylammonium Iodide via Evaporation - Combined Kinetic and Mass Spectrometric Study. *RSC Adv.* **2018**, *8* (52), 29899−29908.

(21) Kroll, M.; Öz, S. D.; Ji, R.; Zhang, Z.; Schramm, T.; Antrack, T.; Olthof, S.; Vaynzof, Y.; Leo, K. Insights into the Evaporation Behaviour of FAI: Material Degradation and Consequences for Perovskite Solar Cells. *Sustain. Energy Fuels* **2022**, *6* (13), 3230−3239.

(22) Roß, M.; Stutz, M. B.; Albrecht, S. Revealing the Role of Methylammonium Iodide Purity on the Vapor-Phase Deposition Process of Perovskites. *Sol. RRL* **2022**, *6* (10), 2200500.

(23) Abzieher, T.; Feeney, T.; Schackmar, F.; Donie, Y. J.; Hossain, I. M.; Schwenzer, J. A.; Hellmann, T.; Mayer, T.; Powalla, M.;

Paetzold, U. W. From Groundwork to Efficient Solar Cells: On the Importance of the Substrate Material in Co-Evaporated Perovskite Solar Cells. *Adv. Funct. Mater.* **2021**, *31* (42), 2104482.
(24) Roß, M.; Gil-Escrig, L.; Al-Ashouri, A.; Tockhorn, P.; Jošt, M.; Rech, B.; Albrecht, S. Co-Evaporated p-i-n Perovskite Solar Cells beyond 20% Efficiency: Impact of Substrate Temperature and Hole-Transport Layer. *ACS Appl. Mater. Interfaces* **2020**, *12* (35), 39261−39272.
(25) Roß, M.; Severin, S.; Stutz, M. B.; Wagner, P.; Köbler, H.; Favin-Lévêque, M.; Al-Ashouri, A.; Korb, P.; Tockhorn, P.; Abate, A.; Stannowski, B.; Rech, B.; Albrecht, S. Co-Evaporated Formamidinium Lead Iodide Based Perovskites with 1000 h Constant Stability for Fully Textured Monolithic Perovskite/Silicon Tandem Solar Cells. *Adv. Energy Mater.* **2021**, *11* (35), 2101460.
(26) Xu, H.; Wu, Y.; Cui, J.; Ni, C.; Xu, F.; Cai, J.; Hong, F.; Fang, Z.; Wang, W.; Zhu, J.; Wang, L.; Xu, R.; Xu, F. Formation and Evolution of the Unexpected PbI2 Phase at the Interface during the Growth of Evaporated Perovskite Films. *Phys. Chem. Chem. Phys.* **2016**, *18* (27), 18607−18613.
(27) Lohmann, K. B.; Patel, J. B.; Rothmann, M. U.; Xia, C. Q.; Oliver, R. D. J.; Herz, L. M.; Snaith, H. J.; Johnston, M. B. Control over Crystal Size in Vapor Deposited Metal-Halide Perovskite Films. *ACS Energy Lett.* **2020**, *5* (3), 710−717.
(28) Yan, S.; Patel, J. B.; Lee, J. E.; Elmestekawy, K. A.; Ratnasingham, S. R.; Yuan, Q.; Herz, L. M.; Noel, N. K.; Johnston, M. B. A Templating Approach to Controlling the Growth of Coevaporated Halide Perovskites. *ACS Energy Lett.* **2023**, *8* (10), 4008−4015.
(29) Chen, B.; Rudd, P. N.; Yang, S.; Yuan, Y.; Huang, J. Imperfections and Their Passivation in Halide Perovskite Solar Cells. *Chem. Soc. Rev.* **2019**, *48* (14), 3842−3867.
(30) Cho, C.; Feldmann, S.; Yeom, K. M.; Jang, Y.-W.; Kahmann, S.; Huang, J.-Y.; Yang, T. C.-J.; Khayyat, M. N. T.; Wu, Y.-R.; Choi, M.; Noh, J. H.; Stranks, S. D.; Greenham, N. C. Efficient Vertical Charge Transport in Polycrystalline Halide Perovskites Revealed by Four-Dimensional Tracking of Charge Carriers. *Nat. Mater.* **2022**, *21* (12), 1388−1395.
(31) Heinze, K. L.; Dolynchuk, O.; Burwig, T.; Vaghani, J.; Scheer, R.; Pistor, P. Importance of Methylammonium Iodide Partial Pressure and Evaporation Onset for the Growth of Co-Evaporated Methylammonium Lead Iodide Absorbers. *Sci. Rep.* **2021**, *11* (1), 15299.
(32) Rothmann, M. U.; Kim, J. S.; Borchert, J.; Lohmann, K. B.; O'Leary, C. M.; Sheader, A. A.; Clark, L.; Snaith, H. J.; Johnston, M. B.; Nellist, P. D.; Herz, L. M. Atomic-Scale Microstructure of Metal Halide Perovskite. *Science* **2020**, *370* (6516), No. eabb5940.
(33) Jacobsson, T. J.; Correa-Baena, J.-P.; Halvani Anaraki, E.; Philippe, B.; Stranks, S. D.; Bouduban, M. E. F.; Tress, W.; Schenk, K.; Teuscher, J.; Moser, J.-E.; Rensmo, H.; Hagfeldt, A. Unreacted PbI_2 as a Double-Edged Sword for Enhancing the Performance of Perovskite Solar Cells. *J. Am. Chem. Soc.* **2016**, *138* (32), 10331−10343.
(34) Roose, B.; Dey, K.; Chiang, Y.-H.; Friend, R. H.; Stranks, S. D. Critical Assessment of the Use of Excess Lead Iodide in Lead Halide Perovskite Solar Cells. *J. Phys. Chem. Lett.* **2020**, *11* (16), 6505−6512.
(35) Li, Y.; Shi, B.; Xu, Q.; Yan, L.; Ren, N.; Chen, Y.; Han, W.; Huang, Q.; Zhao, Y.; Zhang, X. Wide Bandgap Interface Layer Induced Stabilized Perovskite/Silicon Tandem Solar Cells with Stability over Ten Thousand Hours. *Adv. Energy Mater.* **2021**, *11* (48), 2102046.
(36) Yang, X.; Luo, D.; Xiang, Y.; Zhao, L.; Anaya, M.; Shen, Y.; Wu, J.; Yang, W.; Chiang, Y.-H.; Tu, Y.; Su, R.; Hu, Q.; Yu, H.; Shao, G.; Huang, W.; Russell, T. P.; Gong, Q.; Stranks, S. D.; Zhang, W.; Zhu, R. Buried Interfaces in Halide Perovskite Photovoltaics. *Adv. Mater.* **2021**, *33* (7), 2006435.
(37) Leyden, M. R.; Ono, L. K.; Raga, S. R.; Kato, Y.; Wang, S.; Qi, Y. High Performance Perovskite Solar Cells by Hybrid Chemical Vapor Deposition. *J. Mater. Chem. A* **2014**, *2* (44), 18742−18745.
(38) Liu, T.; Lai, H.; Wan, X.; Zhang, X.; Liu, Y.; Chen, Y. Cesium Halides-Assisted Crystal Growth of Perovskite Films for Efficient Planar Heterojunction Solar Cells. *Chem. Mater.* **2018**, *30* (15), 5264−5271.
(39) Xu, J.; Boyd, C. C.; Yu, Z. J.; Palmstrom, A. F.; Witter, D. J.; Larson, B. W.; France, R. M.; Werner, J.; Harvey, S. P.; Wolf, E. J.; Weigand, W.; Manzoor, S.; van Hest, M. F. A. M.; Berry, J. J.; Luther, J. M.; Holman, Z. C.; McGehee, M. D. Triple-Halide Wide-Band Gap Perovskites with Suppressed Phase Segregation for Efficient Tandems. *Science* **2020**, *367* (6482), 1097−1104.
(40) Kim, I. S.; Martinson, A. B. F. Stabilizing Hybrid Perovskites against Moisture and Temperature via Non-Hydrolytic Atomic Layer Deposited Overlayers. *J. Mater. Chem. A* **2015**, *3* (40), 20092−20096.
(41) Boyd, C. C.; Cheacharoen, R.; Leijtens, T.; McGehee, M. D. Understanding Degradation Mechanisms and Improving Stability of Perovskite Photovoltaics. *Chem. Rev.* **2019**, *119* (5), 3418−3451.

https://doi.org/10.1021/acsenergylett.4c02173
ACS Energy Lett. 2024, 9, 5639−5646